Enhanced Oxygen Surface Exchange Kinetics and Stability on Epitaxial La0.8Sr0.2CoO3−δ Thin Films by La0.8Sr0.2MnO3−δ Decoration

ARTICLE *in* THE JOURNAL OF PHYSICAL CHEMISTRY C · JUNE 2014

Impact Factor: 4.77 · DOI: 10.1021/jp502192m

7 AUTHORS, INCLUDING:

Dongkyu Lee
Massachusetts Institute of Technology
21 PUBLICATIONS **84** CITATIONS
SEE PROFILE

Alexis Grimaud
Collège de France
26 PUBLICATIONS **373** CITATIONS
SEE PROFILE

Michael D. Biegalski
Oak Ridge National Laboratory
129 PUBLICATIONS **2,507** CITATIONS
SEE PROFILE

Dane Morgan
University of Wisconsin–Madison
296 PUBLICATIONS **7,273** CITATIONS
SEE PROFILE

THE JOURNAL OF PHYSICAL CHEMISTRY C

Article

pubs.acs.org/JPCC

Enhanced Oxygen Surface Exchange Kinetics and Stability on Epitaxial $La_{0.8}Sr_{0.2}CoO_{3-\delta}$ Thin Films by $La_{0.8}Sr_{0.2}MnO_{3-\delta}$ Decoration

Dongkyu Lee,[†,‡] Yueh-Lin Lee,[†,‡] Alexis Grimaud,[†,‡] Wesley T. Hong,[†,§] Michael D. Biegalski,[∥] Dane Morgan,[⊥] and Yang Shao-Horn*[,†,‡,§]

[†]Electrochemical Energy Laboratory, [‡]Department of Mechanical Engineering, and [§]Department of Materials Science and Engineering, Massachusetts Institute of Technology, 77 Massachusetts Avenue, Cambridge, Massachusetts 02139, United States

[∥]Center for Nanophase Materials Sciences, Oak Ridge National Laboratory, Oak Ridge, Tennessee 37831, United States

[⊥]Department of Materials Science and Engineering, University of Wisconsin−Madison, Madison, Wisconsin 53706, United States

Supporting Information

ABSTRACT: Surface modification of perovskites is a new approach to develop highly active and stable cathodes for solid oxide fuel cells. Here, we report that $La_{0.8}Sr_{0.2}MnO_{3-\delta}$ (LSM82) surface decoration led to markedly enhanced activity and stability for surface exchange kinetics of the $(001)_{pseudocubic}$-oriented epitaxial $La_{0.8}Sr_{0.2}CoO_{3-\delta}$ (LSC82) thin films on (001)-oriented yttria-stabilized zirconia (YSZ). In-plane and out-of-plane strains of the LSC82 films at elevated temperatures determined from in situ high resolution X-ray diffraction were not influenced by LSM82 decoration. Atomic force microscopy and scanning electron microscopy analysis showed that the formation of secondary particles observed upon annealing on the undecorated LSC82 surface was eliminated by the LSM82 decoration, which was accompanied by increased strontium (Sr) on the surface as revealed by auger electron spectroscopy. The enhanced stability of LSM82-decorated LSC82 against surface decomposition is in good agreement with density functional theory (DFT) calculations that showed a considerable energy gain for Mn substitution in LSC82. The surface exchange coefficients (k^q) of LSC82, determined from electrochemical impedance spectroscopy, increased significantly with LSM82 coverage with average thicknesses up to ∼1 nm, while LSM82 thicknesses of ∼3.5 nm and greater reduced k^q. Moreover, LSM82 decoration increased the stability of LSC82 for oxygen surface exchange. Remarkably, the k^q of the LSC82 film with 0.9 nm-thick LSM82 coverage was not changed significantly over 70 h at 550 °C, after which time it exhibited activities 2 orders of magnitude higher than that of the undecorated LSC82. DFT calculations support the hypothesis that the enhanced oxygen surface exchange kinetics and stability of LSM82-decorated LSC82 can be attributed primarily to manganese (Mn) substitution in the LSC82 enabling the stabilization of higher Sr concentration in the perovskite structure near the surface as compared to the undecorated LSC82.

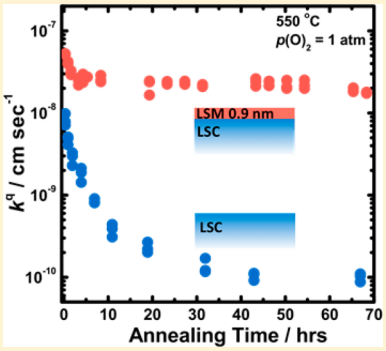

INTRODUCTION

Lowering the operating temperature of solid oxide fuel cells (SOFCs) to the intermediate temperature range (500−750 °C) in the development of advanced SOFCs is hampered by the slow kinetics of the oxygen surface exchange ($O_2 + 4e^- \leftrightarrow 2O^{2-}$) at the cathode.[1−3] Cathode materials based on $La_{1-y}Sr_yMnO_{3-\delta}$ (LSM)[4−8] with high electronic conductivity but low ionic conductivity,[9] which are currently utilized in SOFCs operated at high temperatures such as 1000 °C, have oxygen surface exchange kinetics too slow to achieve efficient SOFCs at intermediate temperatures. Mixed ionic and electronic conductors (MIECs) such as $La_{1-y}Sr_yCoO_{3-\delta}$ (LSC)[10−16] and $La_{1-y}Sr_yCo_{1-x}F_xO_{3-\delta}$ (LSCF)[17−21] perovskite oxides have been intensely studied to promote the oxygen surface exchange kinetics at intermediate temperatures. Recent efforts have been focused on developing advanced cathode materials based on MIECs with surface modification[22−36] to achieve enhanced surface exchange kinetics and stability. For example, Yashiro et al. have reported ∼1 order of magnitude enhancement in activity for the composite cathode screen-printed with the mixture of $La_{0.6}Sr_{0.4}CoO_{3-\delta}$ and $(La_{0.5}Sr_{0.5})_2CoO_{4\pm\delta}$.[35] In addition, LSM has been widely used for surface modification of MIECs.[25,27,29,36] Depositing thin $La_{0.85}Sr_{0.15}MnO_{3-\delta}$ coatings on porous $La_{0.6}Sr_{0.4}Co_{0.2}Fe_{0.8}O_{3-\delta}$ (LSCF6428) electrodes using an infiltration process, Lynch et al.[29] have shown the enhanced surface electrocatalytic activity of decorated LSCF6428 cathodes upon polarization, resulting from a faster surface exchange kinetics relative to uncoated LSCF6428. More recently, Zhu et al.[36] have also shown that the cathodic polarization resistance of LSCF6428 cathode can be reduced by surface modification with a thin and continuous $La_{0.8}Sr_{0.2}MnO_{3-\delta}$ (LSM82) layer via a sol−gel process. Although several studies have shown enhanced cathodic performance by LSM decorations, the influence of LSM on

Received: March 3, 2014
Revised: June 5, 2014
Published: June 6, 2014

the surface chemistry of perovskites that governs oxygen eletrocatalysis at elevated temperatures is poorly understood.

Well-defined single-crystalline perovskite thin films have been used as a model system to develop fundamental understanding into key parameters that govern oxygen surface exchange kinetics.[23,24,31,34,37−44] In particular, the oxygen surface exchange kinetics on epitaxial (001)-oriented $La_{0.8}Sr_{0.2}CoO_{3-\delta}$ (LSC82) thin film surfaces decorated with strontium (hydr)oxide[31] or $(La_{0.5}Sr_{0.5})_2CoO_{4\pm\delta}$ (LSC_{214})[23,24] particles have shown increased activities up to 1 and 3 orders of magnitude, respectively. Our recent study using coherent Bragg rod analysis (COBRA) has revealed the atomic structure and concentrations of the (001)-oriented LSC82 thin film on a $SrTiO_3$ (STO) substrate, which shows pronounced strontium (Sr) segregation toward the LSC82 surface and Sr depletion near the interface between LSC82 and STO.[41] More recently, COBRA has also revealed the markedly higher Sr concentrations at the interface of LSC82 and LSC_{214} and near the surface of LSC_{214} than nominal values, where the enhanced activity for oxygen surface exchange kinetics can be attributed to the increased Sr content in the perovskite structure at the interface and surface regions.[40] In addition, we have shown that heating the (001)-oriented LSC82 surface leads to the formation of surface Sr-enriched particles upon annealing, while the LSC_{214}-decorated LSC82 surface chemistry is stable upon heating.[39] These observations have suggested that the surface decoration can modulate the surface Sr segregation and the surface phase stability, which can greatly influence the oxygen surface exchange kinetics and the surface stability in LSC[45] and LSCF.[25,46] Increasing the Sr content in the perovskite structure, which leads to an increase in vacancy content and an uplift of the O 2p band relative to the Fermi level,[40,47] can increase the surface exchange activity. On the other hand, increasing Sr in the perovskite structure can also destabilize the perovskite phase, leading to thermodynamic driving force to decompose[48,49] and form surface Sr secondary phases.[45] Therefore, stabilizing the perovskite surface to prevent the formation of the Sr-enriched secondary phase plays an important role in achieving and maintaining the high surface exchange kinetics. In this study, we examine whether LSM82 decoration on the LSC82 can alter the surface stability against decomposition to form Sr-enriched particles, and influence the oxygen surface exchange kinetics.

We here employ epitaxial LSC82 thin films with LSM82 surface decoration of varying coverage to investigate how LSM82 decoration can alter the oxygen surface exchange kinetics. Using in situ high-resolution X-ray diffraction (HRXRD), we show that the LSM82 decoration has no influence on the in-plane and out-of-plane strains of the LSC82 films at elevated temperatures. We find that partial LSM82 decoration (~0.1−0.9 nm) can enhance the surface exchange coefficient (k^q) up to 2 orders of magnitude relative to the pristine LSC82 thin film, while full LSM82 coverage (~3.5−10 nm) reduces the k^q values. Auger electron spectroscopy (AES) reveals substantial changes in the surface cationic ratios associated with LSM82 decoration after annealing. Density functional theory (DFT) calculations show A-site cation interdiffusion across the interface between LSM82 and LSC82. The enhanced oxygen surface exchange kinetics of the LSM82-decorated LSC82 thin films can thus be attributed to the stabilization of LSM82-decorated LSC82 surface, where LSC82 surface cationic ratios are changed and the formation of Sr-enriched particles on the surface is suppressed by LSM82 decoration.

EXPERIMENTAL METHODS

Pulsed laser deposition (PLD) was utilized to deposit the epitaxial LSC82 thin films (~85 nm) on yttria-stabilized zirconia (YSZ(001)) with a ~5 nm gadolinium-doped ceria (GDC) buffer layer to prevent the formation of $La_2Zr_2O_7$.[50] Varying thicknesses of LSM82, from partial (~0.1, ~0.3, ~0.9 nm) to full coverage (~3.5 and ~10 nm) were subsequently deposited on top of the LSC82/GDC/YSZ. LSM82 decoration layer thickness was extrapolated from atomic force microscopy (AFM) of the 500 pulses (~3.5 nm) and 1500 pulses (~10 nm) LSM82 coverage on the LSC82 films after microelectrode patterning. The epitaxial LSM82 thin film (~10 nm) on YSZ(001) with a GDC buffer layer was also prepared by PLD. Undecorated LSC82 and LSM82 films were used as reference samples. Details for the LSC, LSM, and GDC PLD target syntheses and PLD deposition process can be found in the Supporting Information.

Oxide phase purity and orientation of the thin film systems were investigated via high-resolution X-ray diffraction (HRXRD) using a four-circle diffractometer (PANalytical, U.S. and Bruker D8, Germany). Measurements were performed in normal and off-normal configurations. The LSC82 in-plane lattice parameter (a lattice parameter) was determined from the off-normal $(202)_{pc}$ peak position (where "pc" denotes the pseudocubic notation), and the c lattice parameter of LSC82 normal to the film surface was determined from the $(002)_{pc}$ peak position. Surface morphology was examined by optical microscopy (Carl Zeiss, Germany) and AFM (Veeco, U.S.). AFM images of as-deposited LSC82 and LSM82-decorated LSC82 films revealed that the surfaces were smooth with the root-mean-square (RMS) roughness values of 0.74−1.12 nm, as shown in Figure 1. The RMS roughness was comparable across all surfaces.

In situ HRXRD was performed on a four-circle diffractometer (PANalytical) in an oxygen partial pressure, $p(O_2)$, of 1 atm and a controlled temperature stage (DHS 900, Anton Paar). Silver paste was used to adhere the thin film sample to the heating plate. The heating rate was ~10 °C min^{-1}, and the

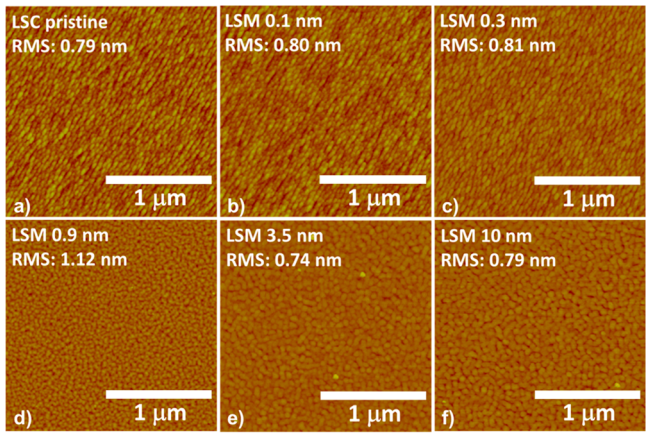

Figure 1. AFM images of (a) as-deposited pristine LSC82 ~85 nm, (b) LSC82 with ~0.1 nm LSM82, (c) LSC82 with ~0.3 nm LSM82, (d) LSC82 with ~0.9 nm LSM82, (e) LSC82 with ~3.5 nm LSM82, and (f) LSC82 with ~10 nm LSM82. RMS roughness values were in the range of 0.74−1.12 nm and comparable across all surfaces.

dx.doi.org/10.1021/jp502192m | J. Phys. Chem. C 2014, 118, 14326−14334

temperature was held for 20 min at each temperature (25, 150, 250, 350, 450, and 550 °C) before XRD data were collected. Sample realignment was conducted at each temperature to maximize the XRD intensities. A full range $\theta-2\theta$ normal scan was collected, and then high-resolution $\theta-2\theta$ normal scans of LSC82 $(002)_{pc}$ and YSZ (002) were collected. Finally, high-resolution off-normal scans of LSC82 $(202)_{pc}$ and YSZ (202) peaks were obtained. As the thermocouple for this experiment was placed inside the heating stage, a small difference between set and actual temperatures on the sample surface cannot be excluded.

Electrochemical impedance spectroscopy (EIS) measurements were performed using a microprobe station (Karl Süss, Germany) connected to a frequency response analyzer (Solartron 1260, U.S.) and dielectric interface (Solartron 1296, U.S.). Thin film microelectrodes ~200 μm in diameter were created by photolithography and acid-etching, and sintered porous Pt deposited on the back-face of the YSZ prior to thin film deposition served as the counter electrode. Temperature was controlled at 550 °C with heating stage (Linkam TS1500, UK), and data were collected between 1 MHz and 1 mHz using a voltage amplitude of 10 mV. EIS testing temperature was calibrated using a thermocouple contacting the thin film surface, and deviation of ±5 °C was observed. EIS experiments were completed in the $p(O_2)$ range from 10^{-3} to 1 atm. EIS data were analyzed using an equivalent circuit shown in the Supporting Information (Figure S4b), from which the ORR resistance (R_{ORR}) and oxygen surface exchange rate were obtained. EIS data of all samples used in this study were found to predominantly exhibit a semicircle in the Nyquist plot. The electrical oxygen surface exchange coefficient (k^q) was calculated from the resistance of the low-frequency semicircle (R_{LF}) using $k^q = RT/4F^2R_{LF}A_{electrode}c_0$,[23,24,31,43,51−53] where R is the universal gas constant (8.314 J mol^{-1} K^{-1}), T is the absolute temperature (823 K), F is Faraday's constant (96 500 C mol^{-1}), $A_{electrode}$ is the area of the microelectrode, and c_0 is the lattice oxygen concentration in LSC82. Details about the EIS testing procedure, data analysis, and c_0 estimation can be found in the Supporting Information.

Auger electron spectroscopy (AES) was conducted using a Physical Electronics 700 Scanning Auger Nanoprobe (PHI, U.S.) operating at an accelerating voltage of 10 kV to analyze the surface chemistry change of the LSM82-decorated LSC82 films after heat treatment. The films were annealed at 550 °C for 6 h in an oxygen partial pressure of 1 atm before AES data were collected. The AES data were collected using two different modes: area mode (three different 10 μm × 10 μm regions selected across a sample) and point mode (two different ~0.45 μm diameter spots selected on a sample) in an ultrahigh vacuum chamber. Elemental quantification of AES spectra utilized relative sensitivity factors (RSFs) of 0.059, 0.027, 0.076, 0.161, and 0.212 for La_{MNN}, Sr_{LMM}, Co_{LMM}, Mn_{LMM}, and O_{KLL}, respectively, as supplied by the AES manufacturer (Physical Electronics). Details about AES measurement and analysis can be found in the Supporting Information.

Calculations for energy of La substituted with Sr (Sr_{La}) in bulk $La_{0.8}Sr_{0.2}CoO_{3-\delta}$ and $La_{0.8}Sr_{0.2}MnO_{3-\delta}$ were performed using a 2 × 2 × 2 pseudocubic supercell structure of $La_{0.75}Sr_{0.25}CoO_3$ (with a_p ($La_{0.75}Sr_{0.25}CoO_3$) = 3.868 Å, where a_p is the GGA+U perovskite lattice constant) and $La_{0.75}Sr_{0.25}MnO_3$ (with a_p ($La_{0.75}Sr_{0.25}MnO_3$) = 3.945 Å) with 2 × 2 × 2 k-point mesh and 450 eV plane-wave energy cutoff. The Sr_{La} substitution energy for $La_{0.75}Sr_{0.25}CoO_3$ ($La_{0.75}Sr_{0.25}MnO_3$) bulk was taken as the difference in energies between a $La_{0.625}Sr_{0.375}CoO_3$ ($La_{0.625}Sr_{0.375}MnO_3$) bulk and a $La_{0.75}Sr_{0.25}CoO_3$ ($La_{0.75}Sr_{0.25}MnO_3$) bulk. The supercell configurations are illustrated in Supporting Information Figure S7. Details of DFT methods are provided in the Supporting Information.

Calculations for energy of mixing of $La_{1-y}Sr_yCo_{1-x}Mn_xO_3$ relative to the $La_{1-y}Sr_yCoO_3$ and $La_{1-y}Sr_yMnO_3$ were performed using the same 2 × 2 × 2 pseudocubic supercell size as was used for LSC and LSM (shown in Supporting Information Figure S7), having a number of lanthanum (La) and Sr concentrations on the A site (y = 0.25, 0.5, and 0.75) and cobalt (Co) and manganese (Mn) concentrations on the B site (x = 0, 0.125, 0.25, 0.375, 0.5, 0.625, 0.75, 0.875, and 1). Fully relaxed calculations were performed to obtain the relaxed volume (Vol) of the 2 × 2 × 2 supercell for extracting the effective lattice constant a_p of the pseudocubic perovskite supercell at different La/Sr and Co/Mn concentrations (a_p = (Vol)$^{1/3}$/2). Internal relaxation was then performed by fixing the supercell lattice constant to $2a_p$ (i.e., 2 × 2 × 2 pseudocubic perovskite supercell) to obtain the DFT total energy. The energy of mixing (ΔE^{MIX} in eV per formula unit) was calculated on the basis of the following equation:

$$\Delta E^{MIX} = E^{DFT}(La_{1-y}Sr_yCo_{1-x}Mn_xO_3) - (1-x) \times E^{DFT}(La_{1-y}Sr_yCoO_3) - x \times E^{DFT}(La_{1-y}Sr_yMnO_3) \quad (1)$$

where $E^{DFT}(La_{1-y}Sr_yCo_{1-x}Mn_xO_3)$, $E^{DFT}(La_{1-y}Sr_yCoO_3)$, and $E^{DFT}(La_{1-y}Sr_yMnO_3)$ are the calculated DFT total energies of $La_{1-y}Sr_yCo_{1-x}Mn_xO_3$, $La_{1-y}Sr_yCoO_3$, and $La_{1-y}Sr_yMnO_3$ normalized as per formula unit, respectively.

RESULTS AND DISCUSSION

Normal XRD data (Figure 2a) of the undecorated LSC82 and LSM82-decorated LSC82 films clearly show the presence of the

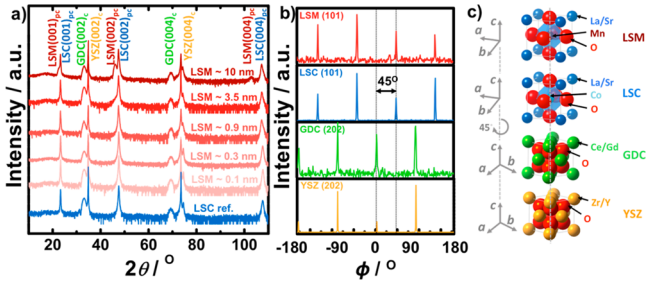

Figure 2. X-ray diffraction (Cu K_α) analysis at room temperature. (a) Normal XRD of the epitaxial LSC82 reference and the LSM82-decorated LSC82 films, (b) off-normal XRD of a similarly prepared sample with a thicker (~10 nm) LSM82 coverage, and (c) schematic of the crystallographic rotational relationships among the $LSM82(001)_{pc}$, $LSC82(001)_{pc}$, $GDC(001)_{cubic}$, and $YSZ(001)_{cubic}$.

$(00l)_{pc}$ (l is integer) peaks of LSC82 and $(00l)_{cubic}$ (l is even) peaks of GDC and YSZ, indicating that the LSC82 film grew epitaxially with the following epitaxial relationships: $(001)_{pc}LSC82//(001)_{cubic}GDC//(001)_{cubic}YSZ$. With LSM82 coverage equal to ~10 nm in thickness, the $(00l)_{pc}$ (l is integer) peaks of LSM82 become visible, which represents $(001)_{pc}LSM82//(001)_{pc}LSC82//(001)_{cubic}GDC//(001)_{cubic}YSZ$. Off-normal phi-scan analysis of the undecorated

dx.doi.org/10.1021/jp502192m | J. Phys. Chem. C 2014, 118, 14326−14334

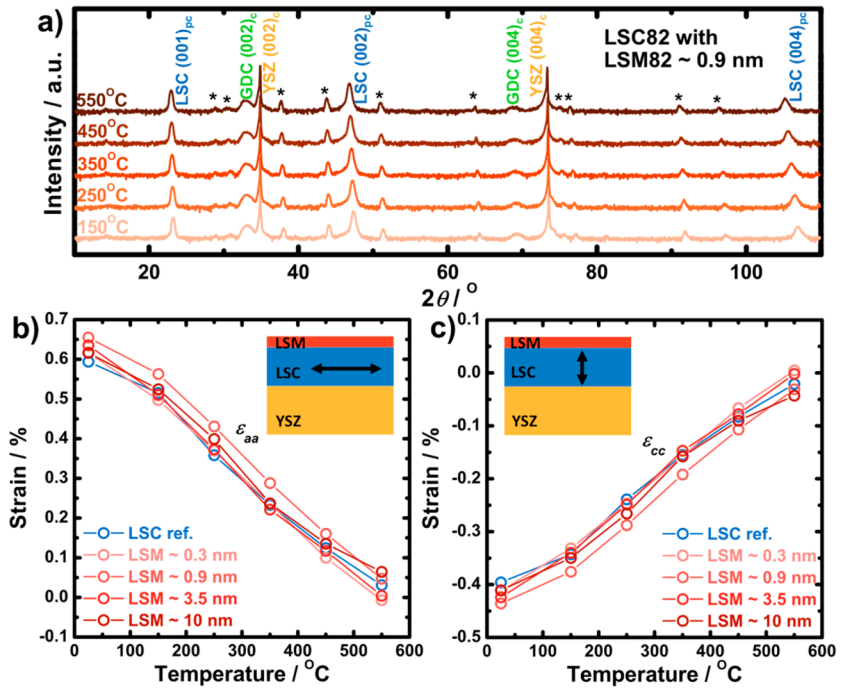

Figure 3. Structural stability and strains of the epitaxial LSC82 with LSM82 coverage (~0.9 nm) thin film. (a) A full-range normal scan in the θ-2θ Bragg–Brentano geometry from 150 to 550 °C, showing no phase change upon heating at a $p(O_2)$ of 1 atm. The starred (*) peaks originated from the heater, and the peaks of the LSC82, GDC, and YSZ are indexed to the pc ($a_{pc} \approx 3.85$ Å[55]), cubic ($a_c \approx 5.42$ Å[57]), and cubic ($a_c \approx 5.15$ Å[58]) structure, respectively. (b) The in-plane strains, ε_{aa}, and (c) the out-of-plane strains, ε_{cc}, of the epitaxial LSC82 and LSM82-decorated LSC82 films as a function of temperature.

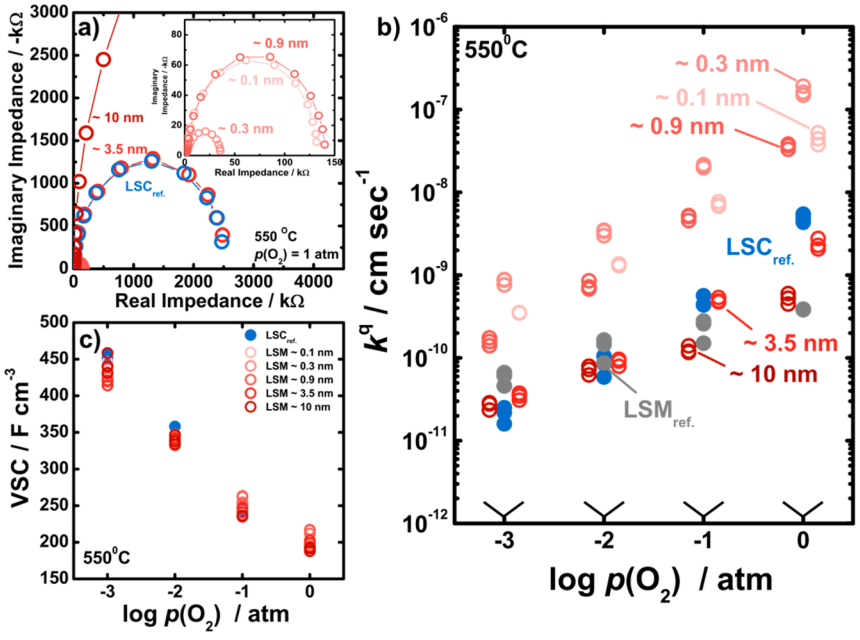

Figure 4. Electrochemical impedance spectroscopy (EIS) results for the undecorated LSM82, LSC82 films and the LSC82 films with ~0.1, ~0.3, ~0.9, ~3.5, and ~10 nm LSM82 decorations at 550 °C. (a) Nyquist plot of the epitaxial LSC82 and the epitaxial LSM82-decorated LSC82 films in 1 atm. Inset shows a magnification of the Nyquist plot of the LSC82 films with partial LSM82 coverage (~0.1, ~0.3, and ~0.9 nm), (b) oxygen partial pressure dependency of the surface exchange coefficients (k^q) of the LSM82, LSC82, and LSM82-decorated LSC82 films calculated from EIS spectra collected at 550 °C, and (c) oxygen partial pressure dependency of volume specific capacitance (VSC) of the epitaxial LSC82 and LSM82-decorated LSC82 films calculated from EIS spectra collected at 550 °C.

LSC82 and LSM82-decorated LSC82 films shows that LSM82 $\{101\}_{pc}$, LSC82 $\{101\}_{pc}$, GDC $\{202\}_{cubic}$, and YSZ $\{202\}_{cubic}$ have strong peaks with 4-fold cubic symmetry (Figure 2b), which reveals the in-plane crystallographic relationships between GDC and YSZ (a cube-on-cube alignment), LSC82 and GDC (an in-plane 45° rotation with $[100]_{pc}$ LSC82// $[110]_{cubic}$ GDC//$[110]_{cubic}$ YSZ), and LSC82 and LSM82 (no rotation with $[100]_{pc}$ LSC82//$[100]_{pc}$ LSM82), as shown in

dx.doi.org/10.1021/jp502192m | J. Phys. Chem. C 2014, 118, 14326–14334

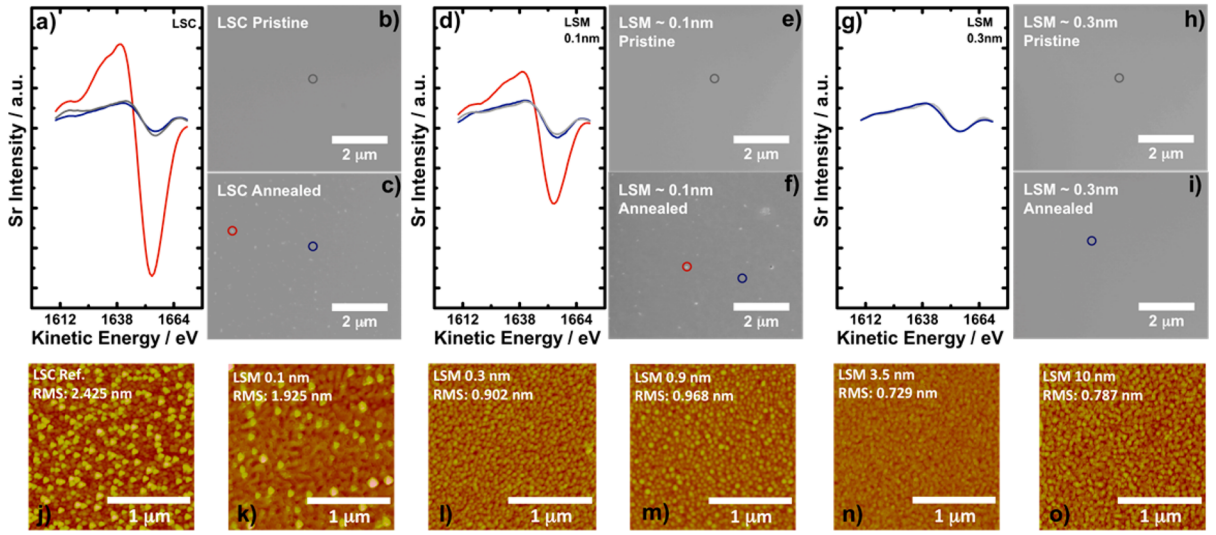

Figure 5. AES, SEM, and AFM analysis for bare LSC82 and LSM82-decorated LSC82 films before and after annealing. Annealing was performed at 550 °C in an oxygen partial pressure of 1 atm. (a) Sr Auger spectra of bare LSC82 thin film probed for as-deposited surface (gray), particles (red), and particle-free surface (blue) after annealing. SEM image of (b) as-deposited and (c) annealed LSC82. (d) Sr Auger spectra of LSC82 with ~0.1 nm LSM82 probed for as-deposited surface (gray), particles (red), and particle-free surface (blue) after annealing. SEM image of (e) as-deposited and (f) annealed LSC82 with ~0.1 nm LSM82. (g) Sr Auger spectra of LSC82 with ~0.3 nm LSM82 probed for as-deposited surface (gray), and annealed surface (blue). No particles were observed. SEM image of (h) as-deposited and (i) annealed LSC82 with ~0.3 nm LSM82. AFM images also showed particle formation on (j) annealed LSC82, (k) annealed LSC82 with ~0.1 nm LSM82, but no particles were observed on (l) annealed LSC82 with ~0.3 nm LSM82, (m) annealed LSC82 with ~0.9 nm LSM82, (n) annealed LSC82 with ~3.5 nm LSM82, or (o) annealed LSC82 with ~10 nm LSM82.

Figure 2c. The relaxed lattice parameters, $\hat{a}$, of the epitaxial LSC82 films with and without LSM82 surface decoration in this study at room temperature did not change significantly with different LSM82 decoration thicknesses, ranging from 3.838–3.843 Å (Supporting Information Table S1). Details about lattice parameter calculation and HRXRD of LSM82 reference film can be found in the Supporting Information.

In situ HRXRD was conducted to show that the undecorated LSC82 and LSM82-decorated LSC82 films were structurally stable upon heating to 550 °C in an oxygen partial pressure of 1 atm. Upon heating to 550 °C, only peak shifts toward low diffraction angles associated with the thermal expansion of LSC82 were observed, as shown in Figure 3a and Supporting Information Figure S2. Both in-plane and out-of-plane strains of LSC82 films were not strongly influenced by the LSM82 coverage, which is supported by the fact that the lattice constant of LSM82 (a_{pc} = 3.89 Å for LSM bulk[54]) is very close to that of LSC82 (a_{pc} ≈ 3.85 Å for LSC bulk[55]). The volumetric thermal expansion coefficients (TECs) of the epitaxial LSC82 films with and without LSM82 decoration (13.8×10^{-6} to 14.9×10^{-6} K^{-1}) were in good agreement with those reported in the literature (14.9×10^{-6} K^{-1} for LSC thin films[38]). In-plane (ε_{aa}) and out-of-plane (ε_{cc}) strains of the epitaxial LSC82 films with and without LSM82 decoration were found to be temperature dependent (Figure 3b and c), which can be attributed to the difference in the thermal expansion coefficients between the LSC82 (14.9×10^{-6} K^{-1}) and YSZ substrate (8.8×10^{-6} K^{-1}).[56] In-plane strains changed from tensile to compressive, while the out-of-plane strains varied from compressive to tensile upon heating. Interestingly, in-plane and out-of-plane strains of the LSC82 films with and without LSM82 coverage at 550 °C were found to be very small (~0.05–0.06%). Details about in situ HRXRD of LSC82 films with LSM82 decoration, temperature-dependent strains, and lattice parameters are provided in the Supporting Information.

EIS data collected from the undecorated LSC82 and LSM82-decorated LSC82 films at 550 °C with an oxygen partial pressure, $p(O_2)$, of 1 atm are shown in Figure 4a. The real impedance of the predominant semicircle decreased significantly with LSM82 coverage less than or equal to ~0.9 nm in thickness, while it increased with larger LSM82 thicknesses. In addition, the predominant semicircle was found to increase with decreasing $p(O_2)$, where EIS data of all samples used in this study were found to show nearly perfect semicircle impedances.[9] Representative EIS data collected from the LSC82 film with ~0.3 nm LSM82 coverage measured at 550 °C as a function of $p(O_2)$ are shown in Supporting Information Figure S4c. Considering the fact that the film thicknesses are much smaller than the critical thickness (estimated to 1 μm for bulk LSC at 550 °C[6]), the $p(O_2)$-dependent impedance responses suggest that the oxygen surface exchange kinetics governs the oxygen electrocatalysis on the film surface. The LSC82 films with partial LSM82 coverage (~0.1, ~0.3, and ~0.9 nm) exhibit enhanced k^q relative to the undecorated LSC82 film by up to nearly 2 orders of magnitude, while the LSC82 films with full LSM82 coverage (~3.5 and ~10 nm) have similar or much lower k^q relative to the undecorated LSC82 film, as shown in Figure 4b. Interestingly, the k^q value of the LSC82 film with ~10 nm LSM82 coverage was found to be comparable to that of the LSM82 reference film. Details of EIS data collected from the LSM82 reference film can be found in the Supporting Information.

The volume specific capacitances (VSCs) extracted from EIS data of the epitaxial LSC82 and LSM82-decorated LSC82 films, corresponding to the change in the oxygen nonstoichiometry (δ) induced by the change in the electrical potential, did not change significantly with LSM82 decoration, as shown in Figure 4c. Indeed, the VSCs in this study were comparable to those of epitaxial LSC82 thin films reported previously.[24,43] This observation indicates that the oxygen content in the LSC82

dx.doi.org/10.1021/jp502192m | J. Phys. Chem. C 2014, 118, 14326–14334

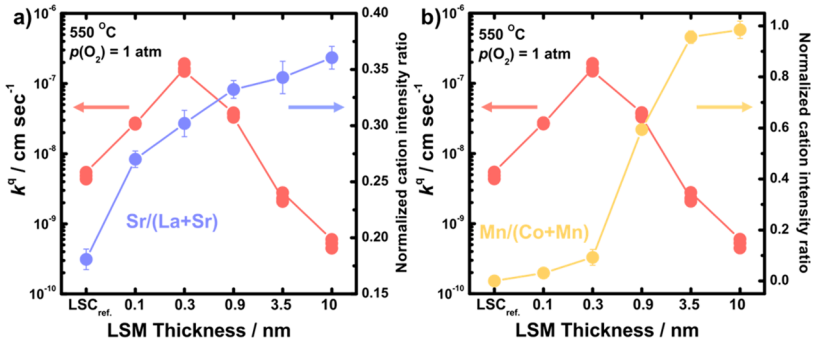

Figure 6. Surface exchange coefficients (k^q) of the LSM82-decorated LSC82 films calculated from EIS spectra collected at 550 °C in a $p(O_2)$ of 1 atm and normalized cation intensity ratios extracted from area mode using AES after annealing at 550 °C in a $p(O_2)$ of 1 atm. (a) k^q (red ●) and normalized La and Sr intensity ratio (blue ●), and (b) k^q (red ●) and normalized Co and Mn intensity ratio (yellow ●) as a function of LSM82 thickness.

films with and without LSM82 coverage does not contribute to the modification of the k^q values observed. Details of VSCs are provided in the Supporting Information.

To investigate the change of surface chemistry and surface morphology as a function of LSM82 thickness, AES and AFM were conducted on the undecorated LSC82 and LSM82-decorated LSC82 films before and after annealing at 550 °C for 6 h in an oxygen partial pressure of 1 atm, as shown in Figure 5. No particles were observed in the SEM micrographs for undecorated LSC82 and LSM82-decorated LSC82 surfaces before annealing, as shown in Figure 5b, e, and h. After annealing, discrete particles were noted on the undecorated LSC82 and LSC82 with ∼0.1 nm LSM82 coverage surfaces (Figure 5c, f, j, and k), whereas no particles were found on LSC82 surfaces with LSM82 decorations thicker than ∼0.3 nm (Figure 5i, l−o). These discrete particles observed on the undecorated LSC82 and ∼0.1 nm-LSM82-decorated surfaces after annealing were found to have higher Sr Auger signals (Figure 5a and d) than the rest of the surface (particle-free surface) as well as the surfaces before annealing, which indicates that Sr-enriched particles were formed after annealing in oxygen. This observation is consistent with our recent in situ studies of surface structure and chemistry changes of LSC82 films[39] and the formation of Sr-enriched particles on annealed LSC64 film surfaces.[45] It is noted that these Sr-enriched particles on the surface of LSC82 were suppressed by LSM decoration. The number density of Sr-enriched particles on the ∼0.1 nm-LSM82-decorated LSC82 surface (1.4 particles per μm^2, ∼3% area coverage) was considerably lower than that of uncoated LSC82 surface (6.1 particles per μm^2, ∼13% area coverage, estimated by averaging particles in three 5 × 5 μm^2 areas in SEM images). LSM82 decoration thicker than ∼0.3 nm resulted in the absence of Sr-enriched particles on the surface, which may result from the incorporation of Sr from LSC82 into the LSM bulk lattice similar to the incorporation of SrO into LSM as suggested previously.[59,60] The chemistry of these Sr-enriched particles is not well understood. Recent COBRA experiments suggest that these Sr-enriched particles on (001)-oriented LSC82 thin films have a composition approaching that of $SrCoO_3$.[41] Nevertheless, the surface of $SrCoO_3$ is most likely decomposed to secondary phases such as $SrO/Sr(OH)_2/SrCO_3$[61,62] and La_2CoO_4,[63] which can greatly impede the surface exchange kinetics.[64]

The increase of the observed k^q values of LSC82 films with partial LSM82 coverage can be attributed partly to the suppression of the Sr-enriched particles on the surface. Partial LSM82 coverage on LSC82 up to 0.9 nm (Figure 4b) enhanced the k^q values of LSC82 films, where the highest k^q value was obtained with LSM82 coverage of ∼0.3 nm. This hypothesis is further supported by the work of Kubicek et al.,[45] which shows a detrimental influence of Sr-enriched particles on the oxygen surface exchange activity of LSC64 films, having improved surface activity by removal of these particles via chemical etching. In contrast, increasing LSM82 coverage on the LSC82 surface from ∼0.9 to ∼10 nm resulted in a reduction in the k^q value, and the 10 nm-LSM82-decorated LSC82 surface had the slowest surface oxygen exchange kinetics approaching that of the LSM82 reference film, which will be discussed later.

The increase of the observed k^q values of LSC82 films with partial LSM82 coverage up to ∼0.9 nm can be also attributed to increased Sr concentration in the perovskite structure near the surface. As shown in Figure 6a, the Sr/(La+Sr) ratios extracted from the AES data using area mode were found to increase with increasing LSM thickness up to ∼0.9 nm, and reach a plateau from ∼0.9 to ∼10 nm considering experimental uncertainty. This hypothesis is in agreement with previous findings that greater Sr concentration on the A-site of the perovskite structure leads to increased oxygen surface exchange kinetics in LSC[47,65,66] and LSM.[5,6] The increased Sr concentration near the surface of the LSC82 with LSM82 decoration may be associated with the thermodynamic driving force of exchanging Sr between LSC82 and LSM82. It should be noted that the energy gain for exchanging a Sr from LSC82 with a La from LSM82 was found to be ∼0.6 eV, calculated from the same method as that used in previous work,[67] where ∼0.9 eV energy gain for exchanging a Sr from $La_{0.75}Sr_{0.25}CoO_{3-\delta}$ with a La from LSC_{214} leads to a large driving force for interdiffusion across the heterostructure interface. Although a more detailed study of the origin of the increased surface Sr concentration is needed, the thermodynamic driving force of exchanging Sr between LSM82 and LSC82 can elucidate the change in the surface Sr concentration. Details of DFT are provided in the Supporting Information.

With LSM82 coverage greater than ∼0.3 nm in thickness, the Mn/(Co+Mn) ratio of LSM82-decorated LSC82 film surfaces significantly increased, as shown in Figure 6b. Assuming that the Sr enrichment above 0.3 nm is enhancing, or at most having minimal impact, on surface exchange, the reduction in the surface oxygen exchange kinetics of LSC82 with LSM82 decoration greater than 0.3 nm can be explained with increasing Mn concentration on the B-site of the perovksite structure near the surface. This hypothesis is supported by the work of De

dx.doi.org/10.1021/jp502192m | J. Phys. Chem. C 2014, 118, 14326−14334

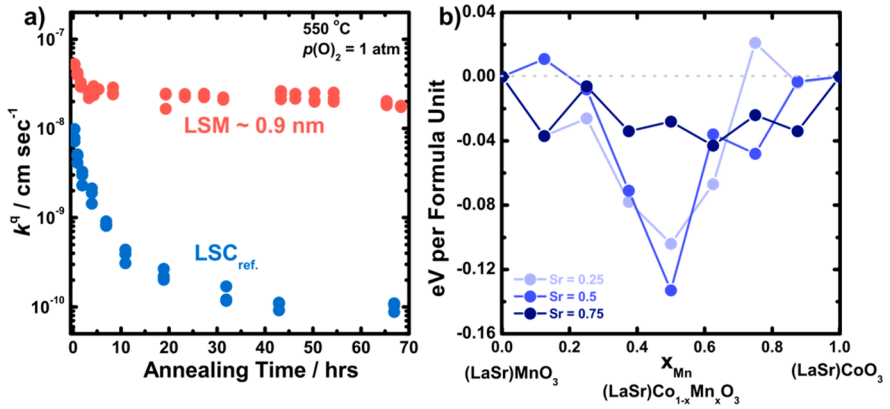

Figure 7. (a) Surface exchange coefficients (k^q) of the LSC82 (blue ●) and LSC82 with ∼0.9 nm LSM82 (red ●) as a function of annealing time. (b) The energy of mixing for $La_{1-y}Sr_yCo_{1-x}Mn_yO_3$ (LSCMO) based on the DFT calculations as a function of Mn concentration with Sr = 0.25 (light blue ●), Sr = 0.5 (blue ●), and Sr = 0.75 (dark blue ●). The supercell configurations used in the DFT calculations are provided in Supporting Information Figure S9. The DFT calculations of energy of mixing suggest that LSCMO can be stabilized with increasing Mn concentration.

Souza and Kilner,[5,6] which shows that the k^* values of $La_{1-y}Sr_yCo_{1-x}Mn_xO_{3\pm\delta}$ (LSCMO) decrease with increasing Mn concentration. Details of AES analysis and AES spectra of each film can be found in the Supporting Information.

LSM82 coverage also enhanced the stability of the LSC82 thin film for oxygen surface exchange kinetics, as shown in Figure 7a. The LSC82 film with LSM82 coverage ∼0.9 nm was found to show stable k^q values for over 70 h, whereas the k^q values of the undecorated LSC82 were reduced significantly (∼2 orders of magnitude) over 20 h. Moreover, as shown in Supporting Information Figure S8, LSM82 coverage was found to lead to higher time-dependent stability of LSC82 relative to the LSC_{214}-decorated LSC82. The enhanced oxygen surface exchange kinetics and stability of the LSM82-decorated LSC82 can be attributed primarily to manganese (Mn) substitution in the LSC82, enabling the stabilization of higher Sr concentration in the perovskite structure near the surface as compared to the undecorated LSC82. This hypothesis is consistent with expectations from experimental and DFT data. First, it has been shown previously that SrO is more stable (has lower activity) in LSM than in LSC at 800 °C,[68] which suggests that alloying LSC with LSM would stabilize it against forming SrO. Furthermore, DFT calculations of the energy of mixing for LSCMO (Figure 7b) show that alloying LSC and LSM (at fixed Sr content) to form LSCMO is energetically favorable over a wide range of Sr concentrations, where the greatest stabilization is around Mn concentration (x_{Mn}) equal to 0.5 with mixing energy of −0.10, −0.13, and −0.04 eV per formula unit at Sr = 0.25, 0.5, and 0.75, respectively. Assuming no large stabilization of decomposition products is enabled by the presence of both Mn and Co, the greater stability of SrO in LSM versus LSC and the negative mixing enthalpy of LSM and LSC support the hypothesis that the LSCMO perovskite structure will be more stable than LSC against decomposition to form surface secondary Sr-rich phases. This hypothesis is also supported by the absence of surface Sr-enriched particles on LSC82 with LSM82 coverage seen in this work (Figure 5). As greater Sr concentration from Auger analysis was correlated with faster surface exchange kinetics, it is proposed that having higher Sr concentration in the perovskite structure near the surface of LSCMO, and its stability against surface decomposition to form secondary Sr-enriched particles, are responsible for the enhanced activity and stability for surface exchange kinetics of LSC82 with LSM82 decoration, respectively.

CONCLUSIONS

We show that LSM82 surface decoration coverage can strongly affect the surface exchange kinetics and the surface stability of epitaxial LSC82 thin films. The k^q values of the epitaxial LSC82 thin films with partial LSM coverage (∼0.1, ∼0.3, ∼0.9 nm) are significantly enhanced relative to the undecorated LSC82 film, while those with full LSM coverage (∼3.5 and ∼10 nm) are similar or diminished. AFM and SEM show the suppression of surface Sr-enriched particles by LSM82, and Auger results reveal increasing surface Sr and Mn with increasing LSM82 coverage. It is postulated that the enhanced oxygen surface exchange kinetics and stability of LSM82-decorated LSC82 can be attributed primarily to the manganese (Mn) substitution in the LSC82 stabilizing higher Sr concentration in the perovskite structure near the surface as compared to the undecorated LSC82. Our results demonstrate that small changes in the surface chemistry of perovskites can yield significant increases in the oxygen surface exchange kinetics and the surface stability with control of surface decoration thickness, which can be potentially utilized to develop highly active oxygen surface exchange materials for applications in the field of solid-state electrochemistry such as intermediate temperature SOFC cathodes, solid-electrolyte-based sensors, and oxygen conducting membranes.

ASSOCIATED CONTENT

Supporting Information

Details of sample preparation, EIS testing, HRXRD, in situ XRD, AES, and DFT. This material is available free of charge via the Internet at http://pubs.acs.org.

AUTHOR INFORMATION

Corresponding Author

*E-mail: shaohorn@mit.edu.

Notes

The authors declare no competing financial interest.

ACKNOWLEDGMENTS

We would like to thank the King Fahd University of Petroleum and Minerals in Dharam, Saudi Arabia for partial funding of the research reported in this Article through the Center for Clean Water and Clean Energy at MIT and KFUPM. This work was also partially supported by the Department of Energy (DOE),

National Energy Technology Laboratory (NETL), Solid State Energy Conversion Alliance (SECA) Core Technology Program, Funding Opportunity Number DEFE0009435. Computations in this work benefited from the use of the Extreme Science and Engineering Discovery Environment (XSEDE), which is supported by National Science Foundation grant number OCI-1053575. The PLD was conducted at the Center for Nanophase Materials Sciences, which is sponsored at Oak Ridge National Laboratory by the Scientific User Facilities Division, Office of Basic Energy Sciences, U.S. Department of Energy. We thank Dr. Zhenxing Feng for his help with sample preparation for this study.

REFERENCES

(1) Shao, Z. P.; Haile, S. M. A High-Performance Cathode for the Next Generation of Solid-Oxide Fuel Cells. *Nature* **2004**, *431*, 170−173.

(2) Steele, B. C. H.; Heinzel, A. Materials for Fuel-Cell Technologies. *Nature* **2001**, *414*, 345−352.

(3) Yang, L.; Zuo, C. D.; Wang, S. Z.; Cheng, Z.; Liu, M. L. A Novel Composite Cathode for Low-Temperature SOFCs based on Oxide Proton Conductors. *Adv. Mater.* **2008**, *20*, 3280−3283.

(4) da Conceicao, L.; Silva, C. R. B.; Ribeiro, N. F. P.; Souza, M. Influence of the Synthesis Method on the Porosity, Microstructure and Electrical Properties of $La_{0.7}Sr_{0.3}MnO_3$ Cathode Materials. *Mater. Charact.* **2009**, *60*, 1417−1423.

(5) De Souza, R. A.; Kilner, J. A. Oxygen Transport in $La_{1-x}Sr_xMn_{1-y}Co_yO_{3\pm\delta}$ Perovskites - Part I. Oxygen Tracer Diffusion. *Solid State Ionics* **1998**, *106*, 175−187.

(6) De Souza, R. A.; Kilner, J. A. Oxygen Transport in $La_{1-x}Sr_xMn_{1-y}Co_yO_{3\pm\delta}$ Perovskites -Part II. Oxygen Surface Exchange. *Solid State Ionics* **1999**, *126*, 153−161.

(7) Endo, A.; Fukunaga, H.; Wen, C.; Yamada, K. Cathodic Reaction Mechanism of Dense $La_{0.6}Sr_{0.4}CoO_3$ and $La_{0.81}Sr_{0.09}MnO_3$ Electrodes for Solid Oxide Fuel Cells. *Solid State Ionics* **2000**, *135*, 353−358.

(8) Ioroi, T.; Hara, T.; Uchimoto, Y.; Ogumi, Z.; Takehara, Z. Preparation of Perovskite-Type $La_{1-x}Sr_xMnO_3$ Films by Vapor-Phase Processes and Their Electrochemical Properties. *J. Electrochem. Soc.* **1997**, *144*, 1362−1370.

(9) Adler, S. B. Factors Governing Oxygen Reduction in Solid Oxide Fuel Cell Cathodes. *Chem. Rev.* **2004**, *104*, 4791−4843.

(10) Adler, S. B. Mechanism and Kinetics of Oxygen Reduction on Porous $La_{1-x}Sr_xCoO_{3-\delta}$ Electrodes. *Solid State Ionics* **1998**, *111*, 125−134.

(11) Berenov, A. V.; Atkinson, A.; Kilner, J. A.; Bucher, E.; Sitte, W. Oxygen Tracer Diffusion and Surface Exchange Kinetics in $La_{0.6}Sr_{0.4}CoO_{3-\delta}$. *Solid State Ionics* **2010**, *181*, 819−826.

(12) Kawada, T.; Suzuki, J.; Sase, M.; Kaimai, A.; Yashiro, K.; Nigara, Y.; Mizusaki, J.; Kawamura, K.; Yugami, H. Determination of Oxygen Vacancy Concentration in a Thin Film of $La_{0.6}Sr_{0.4}CoO_{3-\delta}$ by an Electrochemical Method. *J. Electrochem. Soc.* **2002**, *149*, E252−E259.

(13) Kilner, J. A.; DeSouza, R. A.; Fullarton, I. C. Surface Exchange of Oxygen in Mixed Conducting Perovskite Oxides. *Solid State Ionics* **1996**, *86*, 703−709.

(14) Mizusaki, J.; Mima, Y.; Yamauchi, S.; Fueki, K.; Tagawa, H. Nonstoichiometry of the Perovskite-Type Oxides $La_{1-x}Sr_xCoO_{3-\delta}$. *J. Solid State Chem.* **1989**, *80*, 102−111.

(15) Sathe, V. G.; Pimpale, A. V.; Siruguri, V.; Paranjpe, S. K. Neutron Diffraction Studies of Perovskite-Type Compounds $La_{1-x}Sr_xCoO_3$ (x = 0.1, 0.2, 0.3, 0.4, 0.5). *J. Phys.: Condens. Matter* **1996**, *8*, 3889−3896.

(16) van Doorn, R. H. E.; Fullarton, I. C.; deSouza, R. A.; Kilner, J. A.; Bouwmeester, H. J. M.; Burggraaf, A. J. Surface Oxygen Exchange of $La_{0.3}Sr_{0.7}CoO_{3-\delta}$. *Solid State Ionics* **1997**, *96*, 1−7.

(17) Bae, J. M.; Steele, B. C. H. Properties of $La_{0.6}Sr_{0.4}Co_{0.2}Fe_{0.8}O_{3-\delta}$ (LSCF) Double Layer Cathodes on Gadolinium-Doped Cerium Oxide (CGO) Electrolytes - I. Role of SiO_2. *Solid State Ionics* **1998**, *106*, 247−253.

(18) Esquirol, A.; Brandon, N. P.; Kilner, J. A.; Mogensen, M. Electrochemical Characterization of $La_{0.6}Sr_{0.4}Co_{0.2}Fe_{0.8}O_3$ Cathodes for Intermediate-Temperature SOFCs. *J. Electrochem. Soc.* **2004**, *151*, A1847−A1855.

(19) Hashimoto, S.; Fukuda, Y.; Kuhn, M.; Sato, K.; Yashiro, K.; Mizusaki, J. Oxygen Nonstoichiometry and Thermo-Chemical Stability of $La_{0.6}Sr_{0.4}Co_{1-y}Fe_yO_{3-\delta}$ (y = 0.2, 0.4, 0.6, 0.8). *Solid State Ionics* **2010**, *181*, 1713−1719.

(20) Tai, L. W.; Nasrallah, M. M.; Anderson, H. U.; Sparlin, D. M.; Sehlin, S. R. Structure and Electrical-Properties of $La_{1-x}Sr_xCo_{1-y}Fe_yO_3$. 1. The System $La_{0.8}Sr_{0.2}Co_{1-y}Fe_yO_3$. *Solid State Ionics* **1995**, *76*, 259−271.

(21) Tai, L. W.; Nasrallah, M. M.; Anderson, H. U.; Sparlin, D. M.; Sehlin, S. R. Structure and Electrical-Properties of $La_{1-x}Sr_xCo_{1-y}Fe_yO_3$. 2. The System $La_{1-x}Sr_xCo_{0.2}Fe_{0.8}O_3$. *Solid State Ionics* **1995**, *76*, 273−283.

(22) Chen, J.; Liang, F. L.; Chi, B.; Pu, J.; Jiang, S. P.; Jian, L. Palladium and Ceria Infiltrated $La_{0.8}Sr_{0.2}Co_{0.5}Fe_{0.5}O_{3-\delta}$ Cathodes of Solid Oxide Fuel Cells. *J. Power Sources* **2009**, *194*, 275−280.

(23) Crumlin, E. J.; Ahn, S. J.; Lee, D.; Mutoro, E.; Biegalski, M. D.; Christen, H. M.; Shao-Horn, Y. Oxygen Electrocatalysis on Epitaxial $La_{0.6}Sr_{0.4}CoO_{3-\delta}$ Perovskite Thin Films for Solid Oxide Fuel Cells. *J. Electrochem. Soc.* **2012**, *159*, F219−F225.

(24) Crumlin, E. J.; Mutoro, E.; Ahn, S. J.; La O, G. J.; Leonard, D. N.; Borisevich, A.; Biegalski, M. D.; Christen, H. M.; Shao-Horn, Y. Oxygen Reduction Kinetics Enhancement on a Heterostructured Oxide Surface for Solid Oxide Fuel Cells. *J. Phys. Chem. Lett.* **2010**, *1*, 3149−3155.

(25) Ding, H. P.; Virkar, A. V.; Liu, M. L.; Liu, F. Suppression of Sr Surface Segregation in $La_{1-x}Sr_xCo_{1-y}Fe_yO_{3-\delta}$: A First Principles Study. *Phys. Chem. Chem. Phys.* **2013**, *15*, 489−496.

(26) Liu, M. F.; Ding, D.; Blinn, K.; Li, X. X.; Nie, L. F.; Liu, M. Enhanced Performance of LSCF Cathode Through Surface Modification. *Int. J. Hydrogen Energy* **2012**, *37*, 8613−8620.

(27) Liu, Z.; Liu, M. F.; Yang, L.; Liu, M. L. LSM-Infiltrated LSCF Cathodes for Solid Oxide Fuel Cells. *J. Energy Chem.* **2013**, *22*, 555−559.

(28) Lou, X. Y.; Wang, S. Z.; Liu, Z.; Yang, L.; Liu, M. L. Improving $La_{0.6}Sr_{0.4}Co_{0.2}Fe_{0.8}O_{3-\delta}$ Cathode Performance by Infiltration of a $Sm_{0.5}Sr_{0.5}CoO_{3-\delta}$ Coating. *Solid State Ionics* **2009**, *180*, 1285−1289.

(29) Lynch, M. E.; Yang, L.; Qin, W. T.; Choi, J. J.; Liu, M. F.; Blinn, K.; Liu, M. L. Enhancement of $La_{0.6}Sr_{0.4}Co_{0.2}Fe_{0.8}O_{3-\delta}$ Durability and Surface Electrocatalytic Activity by $La_{0.85}Sr_{0.15}MnO_{3\pm\delta}$ Investigated Using a New Test Electrode Platform. *Energy Environ. Sci.* **2011**, *4*, 2249−2258.

(30) Muranaka, M.; Sasaki, K.; Suzuki, A.; Terai, T. The Effect of LSGM Nanoparticle Dispersion in Ag-LSGM Composite Thin-Film Cathode. *J. Electrochem. Soc.* **2008**, *155*, B860−B863.

(31) Mutoro, E.; Crumlin, E. J.; Biegalski, M. D.; Christen, H. M.; Shao-Horn, Y. Enhanced Oxygen Reduction Activity on Surface-Decorated Perovskite Thin Films for Solid Oxide Fuel Cells. *Energy Environ. Sci.* **2011**, *4*, 3689−3696.

(32) Nie, L. F.; Liu, M. F.; Zhang, Y. J.; Liu, M. L. $La_{0.6}Sr_{0.4}Co_{0.2}Fe_{0.8}O_{3-\delta}$ Cathodes Infiltrated with Samarium-Doped Cerium Oxide for Solid Oxide Fuel Cells. *J. Power Sources* **2010**, *195*, 4704−4708.

(33) Sakito, Y.; Hirano, A.; Imanishi, N.; Takeda, Y.; Yamamoto, O.; Liu, Y. Silver Infiltrated $La_{0.6}Sr_{0.4}Co_{0.2}Fe_{0.8}O_3$ Cathodes for Intermediate Temperature Solid Oxide Fuel Cells. *J. Power Sources* **2008**, *182*, 476−481.

(34) Sase, M.; Hermes, F.; Yashiro, K.; Sato, K.; Mizusaki, J.; Kawada, T.; Sakai, N.; Yokokawa, H. Enhancement of Oxygen Surface Exchange at the Hetero-Interface of $(La,Sr)CoO_3/(La,Sr)_{(2)}CoO_4$ with PLD-Layered Films. *J. Electrochem. Soc.* **2008**, *155*, B793−B797.

(35) Yashiro, K.; Nakamura, T.; Sase, M.; Hermes, F.; Sato, K.; Kawada, T.; Mizusaki, J. Composite Cathode of Perovskite-Related Oxides, $(La,Sr)CoO_{3-\delta}/(La,Sr)_{(2)}CoO_{4-\delta}$, for Solid Oxide Fuel Cells. *Electrochem. Solid-State Lett.* **2009**, *12*, B135−B137.

(36) Zhu, X. B.; Ding, D.; Li, Y. Q.; Lu, Z.; Su, W. H.; Zhen, L. Development of $La_{0.6}Sr_{0.4}Co_{0.2}Fe_{0.8}O_{3-\delta}$ Cathode with an Improved Stability via $La_{0.8}Sr_{0.2}MnO_3$-Film Impregnation. *Int. J. Hydrogen Energy* **2013**, *38*, 5375−5382.
(37) Crumlin, E. J.; Mutoro, E.; Hong, W. T.; Biegalski, M. D.; Christen, H. M.; Liu, Z.; Bluhm, H.; Shao-Horn, Y. In Situ Ambient Pressure X-ray Photoelectron Spectroscopy of Cobalt Perovskite Surfaces Under Cathodic Polarization at High Temperatures. *J. Phys. Chem. C* **2013**, *117*, 16087−16094.
(38) Crumlin, E. J.; Mutoro, E.; Liu, Z.; Grass, M. E.; Biegalski, M. D.; Lee, Y. L.; Morgan, D.; Christen, H. M.; Bluhm, H.; Shao-Horn, Y. Surface Strontium Enrichment on Highly Active Perovskites for Oxygen Electrocatalysis in Solid Oxide Fuel Cells. *Energy Environ. Sci.* **2012**, *5*, 6081−6088.
(39) Feng, Z.; Crumlin, E. J.; Hong, W. T.; Lee, D.; Mutoro, E.; Biegalski, M. D.; Zhou, H.; Bluhm, H.; Christen, H. M.; Shao-Horn, Y. In Situ Studies of the Temperature-Dependent Surface Structure and Chemistry of Single-Crystalline (001)-Oriented $La_{0.8}Sr_{0.2}CoO_{3-\delta}$ Perovskite Thin Films. *J. Phys. Chem. Lett.* **2013**, *4*, 1512−1518.
(40) Feng, Z. X.; Yacoby, Y.; Gadre, M. J.; Lee, Y. L.; Hong, W. T.; Zhou, H.; Biegalski, M. D.; Christen, H. M.; Adler, S. B.; Morgan, D.; et al. Anomalous Interface and Surface Strontium Segregation in $(La_{1-y}Sr_y)_2CoO_{4\pm\delta}/La_{1-x}Sr_xCoO_{3-\delta}$ Heterostructured Thin Films. *J. Phys. Chem. Lett.* **2014**, *5*, 1027−1034.
(41) Feng, Z.; Yacoby, Y.; Hong, W. T.; Zhou, H.; Biegalski, M. D.; Christen, H. M.; Shao-Horn, Y. Revealing the Atomic Structure and Strontium Distribution in Nanometer-Thick $La_{0.8}Sr_{0.2}CoO_{3-\delta}$ Grown on (001)-Oriented $SrTiO_3$. *Energy Environ. Sci.* **2014**, *7*, 1166−1174.
(42) Kumar, A.; Leonard, D.; Jesse, S.; Ciucci, F.; Eliseev, E. A.; Morozovska, A. N.; Biegalski, M. D.; Christen, H. M.; Tselev, A.; Mutoro, E.; et al. Spatially Resolved Mapping of Oxygen Reduction/Evolution Reaction on Solid-Oxide Fuel Cell Cathodes with Sub-10 nm Resolution. *ACS Nano* **2013**, *7*, 3808−3814.
(43) La O, G. J.; Ahn, S. J.; Crumlin, E.; Orikasa, Y.; Biegalski, M. D.; Christen, H. M.; Shao-Horn, Y. Catalytic Activity Enhancement for Oxygen Reduction on Epitaxial Perovskite Thin Films for Solid-Oxide Fuel Cells. *Angew. Chem., Int. Ed.* **2010**, *49*, 5344−5347.
(44) Leonard, D. N.; Kumar, A.; Jesse, S.; Biegalski, M. D.; Christen, H. M.; Mutoro, E.; Crumlin, E. J.; Shao-Horn, Y.; Kalinin, S. V.; Borisevich, A. Y. Nanoscale Probing of Voltage Activated Oxygen Reduction/Evolution Reactions in Nanopatterned $(La_xSr_{1-x})CoO_3$-Cathodes. *Adv. Energy Mater.* **2013**, *3*, 788−797.
(45) Kubicek, M.; Limbeck, A.; Fromling, T.; Hutter, H.; Fleig, J. Relationship Between Cation Segregation and the Electrochemical Oxygen Reduction Kinetics of $La_{0.6}Sr_{0.4}CoO_{3-\delta}$ Thin Film Electrodes. *J. Electrochem. Soc.* **2011**, *158*, B727−B734.
(46) Oh, D.; Gostovic, D.; Wachsman, E. D. Mechanism of $La_{0.6}Sr_{0.4}Co_{0.2}Fe_{0.8}O_3$ Cathode Degradation. *J. Mater. Res.* **2012**, *27*, 1992−1999.
(47) Lee, Y. L.; Kleis, J.; Rossmeisl, J.; Shao-Horn, Y.; Morgan, D. Prediction of Solid Oxide Fuel Cell Cathode Activity with First-Principles Descriptors. *Energy Environ. Sci.* **2011**, *4*, 3966−3970.
(48) Cherepanov, V. A.; Gavrilova, L. Y.; Barkhatova, L. Y.; Voronin, V. I.; Trifonova, M. V.; Bukhner, O. A. Phase Equilibria in the La-Me-Co-O (Me=Ca, Sr, Ba) Systems. *Ionics* **1998**, *4*, 309−315.
(49) Ovenstone, J.; White, J. S.; Misture, S. T. Phase Transitions and Phase Decomposition of $La_{1-x}Sr_xCoO_{3-\delta}$ in Low Oxygen Partial Pressures. *J. Power Sources* **2008**, *181*, 56−61.
(50) Mitterdorfer, A.; Gauckler, L. J. $La_2Zr_2O_7$ Formation and Oxygen Reduction Kinetics of the $La_{0.85}Sr_{0.15}Mn_yO_3$, $O_2(g)$|YSZ System. *Solid State Ionics* **1998**, *111*, 185−218.
(51) Lee, D.; Grimaud, A.; Crumlin, E. J.; Mezghani, K.; Habib, M. A.; Feng, Z. X.; Hong, W. T.; Biegalski, M. D.; Christen, H. M.; Shao-Horn, Y. Strain Influence on the Oxygen Electrocatalysis of the (100)-Oriented Epitaxial $La_2NiO_{4+\delta}$ Thin Films at Elevated Temperatures. *J. Phys. Chem. C* **2013**, *117*, 18789−18795.
(52) Lee, D.; Lee, Y.-L.; Grimaud, A.; Hong, W. T.; Biegalski, M. D.; Morgan, D.; Shao-Horn, Y. Strontium Influence on the Oxygen Electrocatalysis of $La_{2-x}Sr_xNiO_{4\pm\delta}$ ($0.0 \le x_{Sr} \le 1.0$) Thin Films. *J. Mater. Chem. A* **2014**, *2*, 6480−6487.
(53) Maier, J. *Physical Chemistry of Ionic Materials: Ions and Electrons in Solids*; John Wiley: Chichester, England; Hoboken, NJ, 2004; p 537.
(54) Mori, M.; Hiei, Y.; Sammes, N. M.; Tompsett, G. A. Thermal-Expansion Behaviors and Mechanisms for Ca- or Sr-Doped Lanthanum Manganite Perovskites Under Oxidizing Atmospheres. *J. Electrochem. Soc.* **2000**, *147*, 1295−1302.
(55) van Doorn, R. H. E.; Burggraaf, A. J. Structural Aspects of the Ionic Conductivity of $La_{1-x}Sr_xCoO_{3-\delta}$. *Solid State Ionics* **2000**, *128*, 65−78.
(56) Ishihara, T.; Kudo, T.; Matsuda, H.; Takita, Y. Doped $PrMnO_3$ Perovskite Oxide as a New Cathode of Solid Oxide Fuel Cells for Low-Temperature Operation. *J. Electrochem. Soc.* **1995**, *142*, 1519−1524.
(57) Matovic, B.; Boskovic, S.; Zivkovic, L.; Vlajic, M.; Krstic, V. Lattice Parameters of Gd-Doped Ceria Electrolytes. In *Current Research in Advanced Materials and Processes*; Uskokovic, D. P., Milonjic, S. K., Rakovic, D. I., Eds.; Trans Tech Publications Ltd.: Zurich-Uetikon, 2005; Vol. *494*, pp 175−179.
(58) Yashima, M.; Sasaki, S.; Kakihana, M.; Yamaguchi, Y.; Arashi, H.; Yoshimura, M. Oxygen-Induced Structural-Change of the Tetragonal Phase Around the Tetragonal-Cubic Phase-Boundary in ZrO_2-$YO_{1.5}$ Solid-Solutions. *Acta Crystallogr., Sect. B* **1994**, *50*, 663−672.
(59) Jiang, S. P. Activation, Microstructure, and Polarization of Solid Oxide Fuel Cell Cathodes. *J. Solid State Electrochem.* **2007**, *11*, 93−102.
(60) Wang, W.; Jiang, S. P. A Mechanistic Study on the Activation Process of (La, Sr)MnO_3 Electrodes of Solid Oxide Fuel Cells. *Solid State Ionics* **2006**, *177*, 1361−1369.
(61) Reichenbach, H. M.; McGinn, P. J. Combinatorial Solution Synthesis and Characterization of Complex Oxide Catalyst Powders Based on the $LaMO_3$ System. *Appl. Catal., A* **2003**, *244*, 101−114.
(62) Karvonen, L.; Yoon, S. H.; Hug, P.; Yamauchi, H.; Weidenkaff, A.; Karppinen, M. The n=3 Member of the $SrCoO_{(3n-1)/n}$ Series of Layered Oxygen-Defect Perovskites. *Mater. Res. Bull.* **2011**, *46*, 1340−1345.
(63) Petrov, A. N.; Cherepanov, V. A.; Kononchuk, O. F.; Gavrilova, L. Y. Oxygen Nonstoichiometry of $La_{1-x}Sr_xCoO_{3-\delta}$ ($0 < x \le 0.6$). *J. Solid State Chem.* **1990**, *87*, 69−76.
(64) Fischer, E.; Shen, W. D.; Hertz, J. L. Measurement of the Surface Exchange and Diffusion Coefficients of Thin Film $LaCoO_3$ and $SrCoO_x$. *J. Electroceram.* **2012**, *29*, 262−269.
(65) Horita, T.; Yamaji, K.; Sakai, N.; Yokokawa, H.; Weber, A.; Ivers-Tiffee, E. Oxygen Reduction Mechanism at Porous $La_{1-x}Sr_xCoO_{3-\delta}$ Cathodes/$La_{0.8}Sr_{0.2}Ga_{0.8}Mg_{0.2}O_{2.8}$ Electrolyte Interface for Solid Oxide Fuel Cells. *Electrochim. Acta* **2001**, *46*, 1837−1845.
(66) Hwang, J.; Lee, H.; Yoon, K. J.; Lee, H. W.; Kim, B. K.; Lee, J. H.; Son, J. W. Study on the Electrode Reaction Mechanism of Pulsed-Laser Deposited Thin-Film $La_{1-x}Sr_xCoO_{3-\delta}$ (x=0.2. 0.4) Cathodes. *J. Electrochem. Soc.* **2012**, *159*, F639−F643.
(67) Gadre, M. J.; Lee, Y. L.; Morgan, D. Cation Interdiffusion Model for Enhanced Oxygen Kinetics at Oxide Heterostructure Interfaces. *Phys. Chem. Chem. Phys.* **2012**, *14*, 2606−2616.
(68) Yokokawa, H.; Sakai, N.; Horita, T.; Yamaji, K.; Brito, M. E.; Kishimoto, H. Thermodynamic and Kinetic Considerations on Degradations in Solid Oxide Fuel Cell Cathodes. *J. Alloys Compd.* **2008**, *452*, 41−47.